Rapid strain accumulation on the Ashkabad fault (Turkmenistan) from atmosphere-corrected InSAR

R. J. Walters,[1,2] J. R. Elliott,[1] Z. Li,[3] and B. Parsons[1]

[1] We have measured interseismic deformation across the Ashkabad strike-slip fault using 13 Envisat interferograms covering a total effective timespan of ~30 years. Atmospheric contributions to phase delay are significant and variable due to the close proximity of the Caspian Sea. In order to retrieve the pattern of strain accumulation, we show it is necessary to use data from Envisat's Medium-Resolution Imaging Spectrometer (MERIS) instrument, as well as numerical weather model outputs from the European Centre for Medium-Range Weather Forecasts (ECMWF), to correct interferograms for differences in water vapor and atmospheric pressure, respectively. This has enabled us to robustly estimate the slip rate and locking depth for the Ashkabad fault using a simple elastic dislocation model. Our data are consistent with a slip rate of 5–12 mm/yr below a locking depth of 5.5–17 km for the Ashkabad fault, and synthetic tests support the magnitude of the uncertainties on these estimates. Our estimate of slip rate is 1.25–6 times higher than some previous geodetic estimates, with implications for both seismic hazard and regional tectonics, in particular supporting fast relative motion between the South Caspian Block and Eurasia. This result reinforces the importance of correcting for atmospheric contributions to interferometric phase for small strain measurements. We also attempt to validate a recent method for atmospheric correction based on ECMWF ERA-Interim model outputs alone and find that this technique does not work satisfactorily for this region when compared to the independent MERIS estimates.

1. Introduction

[2] The right-lateral Ashkabad strike-slip fault is located along the northeastern edge of the Kopeh Dagh mountains on the Iran-Turkmenistan border and represents the northernmost boundary of significant deformation from the Arabia-Eurasia collision at this longitude (54°E–57°E). The fault separates the Turkmenistan platform, which is part of stable Eurasia, from the South Caspian Region and from the deforming region of north-east Iran (Figure 1).

[3] The Ashkabad fault is recognized as an important component of regional tectonic models [e.g., *Hollingsworth et al.*, 2008; *Copley and Jackson*, 2006; *Djamour et al.*, 2010] and also poses a significant seismic hazard to a growing urban population in north-east Iran and southern Turkmenistan. The fault has been suggested as a possible source for the damaging 1948 M 7.3 Ashkabad earthquake, although ground deformation measurements [*Tchalenko*, 1975] and seismology [*McKenzie*, 1972] are ambiguous about whether the earthquake occurred as dextral slip on the Ashkabad fault, or as reverse slip on a parallel, SSW-dipping thrust. The exact death toll from this earthquake is unknown, but it is thought that between 10,000 and 176,000 people were killed in Ashkabad city and surrounding Turkmen settlements.

[4] However, despite the Ashkabad fault being a potential source for the 1948 earthquake and its importance in regional tectonic models, the fault's slip rate and therefore also the seismic hazard that it represents are not well known. GPS data in north-east Iran are sparse, and there are no well-constrained geological or Quaternary slip rate estimates for the fault. *Masson et al.* [2007] directly estimated a slip rate of 2–4 mm/yr for the Ashkabad fault from the motion of a single GPS station in north-east Iran, SHIR, relative to Eurasia. *Lyberis and Manby* [1999] proposed a geological slip rate of 6.5–7.5 mm/yr for the fault, based on an estimated right-lateral displacement across the Kopeh Dagh over the last ~5 Ma.

Additional supporting information may be found in the online version of this article.
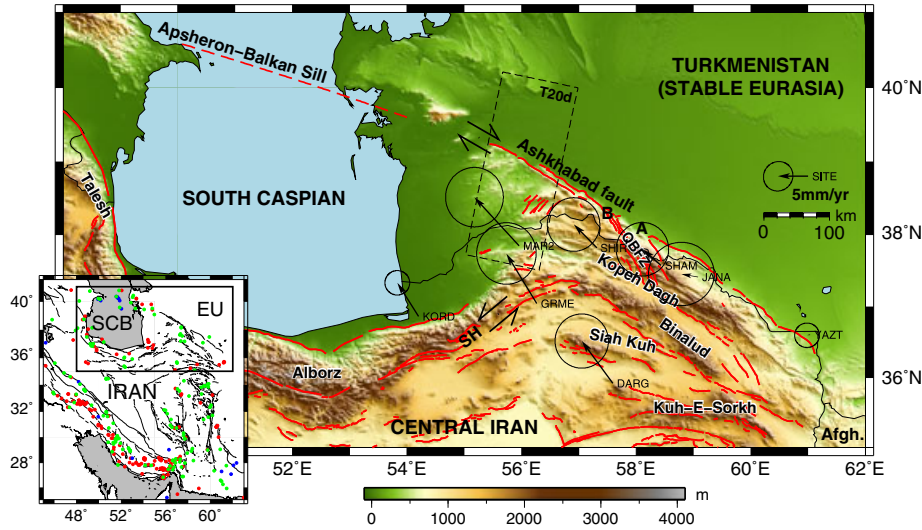[1]COMET+, Department of Earth Sciences, University of Oxford, Oxford, UK.
[2]Now at COMET+, School of Earth and Environment, University of Leeds, Leeds, UK.
[3]COMET+, School of Geographical and Earth Sciences, University of Glasgow, Glasgow, UK.

Corresponding author: R. J. Walters, COMET+, School of Earth and Environment, University of Leeds, Leeds LS2 9JT, UK. (r.j.walters@leeds.ac.uk)

Figure 1. Map of study region. Dashed box shows the footprint of a ~300 km long section of Envisat track T20d used in this study. GPS vectors in a fixed-Eurasia reference frame with 2-sigma error ellipses from *Tavakoli* [2007] are also marked, and active faults are shown in red [*Walker et al.*, 2009]. Large black strike-slip arrows show direction of slip on the Ashkabad fault and the Sharud shear zone (SH). Ashkabad City is marked by the letter A, and the town of Bakharden is marked by the letter B. QBFZ is the Quchan-Bakhardan Fault Zone. Inset panel shows regional map with active faults in black. Red, blue, and green dots show thrust, normal, and strike-slip earthquakes, respectively, in the period 1976–2011, from the gCMT catalog [*Ekström et al.*, 2012]. SCB is the South Caspian Block, and EU is Eurasia. The black box shows the location of the main panel.

[5] In this study, we use Interferometric Synthetic Aperture Radar (InSAR) to directly estimate the slip rate on the Ashkabad fault. However, we find that atmospheric delays to the radar signal are large in this region, obscuring any interseismic tectonic signal, so we first correct for differences in water vapor and atmospheric pressure before interpreting our data in terms of tectonic deformation.

2. Tectonic Setting

[6] Recent GPS measurements show that Arabia-Eurasia N-S convergence at the longitude of north-east Iran (56°E–60°E) is around 25 mm/yr [*Vernant et al.*, 2004; *Masson et al.*, 2007]. These data sets also show that the majority of this motion is taken up in southern Iran by the Zagros fold and thrust belt and by the Makran subduction zone, and that the Kuh-E Sorkh, Siah Kuh, Binalud, and Kopeh Dagh mountain ranges of north-east Iran (Figure 1) only accommodate around 6 mm/yr of this N-S shortening. The South Caspian region moves independently of both north-east Iran and Eurasia and is suggested to be a rigid block based on a lack of internal seismicity [*Jackson and McKenzie*, 1984]. From simple plate-circuit closure models, the South Caspian is thought to be moving to the NW at around 7–10 mm/yr, during the early stages of subduction under the Apsheron-Balkan Sill [*Jackson et al.*, 2002].

[7] The Kopeh Dagh is the northernmost of north-east Iran's mountain belts and is a 120° trending, ~700 km long range that extends from the Caspian Sea in the west to the Afghanistan border in the east. The seismicity along the whole mountain range indicates strain "partitioning" of oblique right-lateral shortening into thrust and strike-slip components, taking place on spatially separate faults [*Jackson et al.*, 2002]. Styles of deformation vary strongly along strike, however, and *Hollingsworth et al.* [2006] define three distinct regions of the Kopeh Dagh; east, west, and central.

[8] East of ~59°E, the Kopeh Dagh have their highest peaks, and GPS measurements show 2 mm/yr N-S shortening between Iran and Eurasia across this section of the mountain range [*Masson et al.*, 2007]. This shortening appears to be partitioned into range-parallel thrusts and right-lateral strike-slip faults.

[9] West of 57°E, the topography across the Kopeh Dagh becomes gradually more subdued as the tectonic structures get progressively buried with sediment toward the Caspian coast [*Lyberis and Manby*, 1999], and the right-lateral Ashkabad fault is the dominant feature in the geomorphology, following the Kopeh Dagh range front. However, thrust faulting is still important in this region, as evidenced by the step in topography across the Ashkabad fault and also by the seismicity [*Jackson et al.*, 2002]. Here right-lateral slip on the Ashkabad fault and slip on range-parallel thrusts accommodates the motion between Eurasia and the South Caspian Block. The Ashkabad fault, together with the left-lateral Sharud fault zone, has been suggested as facilitating the north-westward extrusion of the South Caspian Block [*Jackson et al.*, 2002].

[10] Between 57°E and 59°E, the relative motion of the South Caspian Block away from north-east Iran causes the central portion of the Kopeh Dagh to experience range-parallel extension in addition to the N-S convergence between Iran and Eurasia. *Hollingsworth et al.* [2006] suggest that both E-W extension and N-S compression are

Table 1. SAR Data Used in This Study and Cloud Coverage of the Swath in %[a]

Acq. No.	Date (yymmdd)	Cloud Cover (%)
1	030709	18
2	030917	2
3	031022	3
4	031126	0
5	040310	94
6	040901	1
7	041215	100
8	050223	91
9	050330	70
10	050608	74
11	050713	42
12	051026	34
13	060208	92
14	070822	58
15	071031	0
16	071205	63
17	080109	85
18	080213	100
19	080423	0
20	080528	N/A
21	090513	50
22	090617	16
23	090722	40
24	090826	0
25	090930	15
26	091104	N/A
27	091209	98
28	100217	N/A
29	100428	37
30	100707	9
31	100811	5
32	100915	100

[a]Cloud coverage is defined as the proportion of a 400 km long and 100 km-wide swath on track 20, centered on the Ashkabad fault, that is covered by the official European Space Agency (ESA) Medium-Resolution Imaging Spectrometer (MERIS) cloud mask. N/A refers to dates for which no MERIS data is available.

accommodated by anticlockwise rotation on a series of NNW-striking right-lateral strike-slip faults. This region is termed the Quchan-Bakhardan Fault Zone (QBFZ).

[11] An alternative tectonic model for this region is proposed by *Shabanian et al.* [2009], who suggest that the right-lateral strike-slip faults of the QBFZ do not rotate but instead accommodate the north-westward translation of Iran relative to Eurasia.

3. Construction of Interferograms and Atmospheric Contamination

[12] A total of 32 Envisat SAR acquisitions were available for descending track 20, which covers the western Kopeh Dagh, where the Ashkabad fault separates Eurasia and the South Caspian Block (Table 1). The InSAR data were processed from raw data products using the Jet Propulsion Laboratory/Caltech Repeat Orbit Interferometry Package (ROI_PAC) v3.01 [*Rosen et al.*, 2004]. The interferograms were corrected for orbital effects using DORIS (Doppler Orbitography and Radiopositioning Integrated by Satellite) orbits from the European Space Agency, and effects of topography were removed from the interferograms using a filled 3 arc sec (~90 m) resolution Shuttle Radar Topography Mission (SRTM) digital elevation

model (DEM) [*Farr et al.*, 2007] obtained from the Consultative Group on International Agricultural Research's Consortium for Spatial Information (CGIAR-CSI, http://srtm.csi.cgiar.org). Each interferogram was downsampled during processing to 32 looks in range and 160 looks in azimuth (640 m × 640 m), filtered using a weighted power spectrum filter [*Goldstein and Werner*, 1998] to improve the signal-to-noise ratio, and unwrapped using the branch-cut method. Errors introduced during automatic unwrapping were fixed manually.

[13] From inspection of preliminary interferograms, we suspected that they contained large magnitude atmospheric signals, evidenced by strong correlations between interferometric phase and topography interpreted as stratified atmospheric effects [*Massonnet and Feigl*, 1998], and by the presence of short-wavelength signals interpreted as turbulent atmospheric effects [*Hanssen*, 2001]. To estimate the magnitude of the atmospheric signals we should expect to see in interferograms produced from our data set (Table 1), we estimated phase delay maps using the ERA-Interim global atmospheric model [*Dee et al.*, 2011] obtained from the European Centre for Medium-Range Weather Forecasts (ECMWF). To estimate the combined delay from differences in water vapor (wet delay) and atmospheric pressure (dry delay), we first created delay maps using the method of *Doin et al.* [2009] and *Jolivet et al.* [2011]. The ERA-Interim atmospheric model provides estimates of 16 meteorological parameters including temperature, relative humidity, and geopotential, at 6 h intervals from 1989 onward. Spatially, the outputs are given at grid nodes with ~75 km horizontal spacing, and at 37 pressure levels between ~0 and 50 km above sea level. Atmospheric delay maps are calculated by producing vertical profiles of total path delay at ~75 km resolution using the atmospheric delay formulations of *Baby et al.* [1988], interpolating these horizontally and vertically with bilinear and spline interpolation functions, respectively, and then using a DEM to find the delay at the correct elevation for each point at the surface.

[14] We produced delay maps for each possible interferogram (i.e., each combination of acquisition dates), interpolated at 1.6 km resolution, and then found the range of values across each delay map. This range is an estimate of the maximum atmospheric signal expected in any one interferogram, as the spatial variability of delay across the scene is the important factor, not absolute values of delay. For the 32 SAR acquisitions in our scene, the 992 possible interferograms had an average maximum atmospheric line-of-sight (LOS) signal of 6.7 cm (Figure 3). This is significantly larger than the interseismic signal expected in any one interferogram (0.4–1.5 cm LOS for slip rates of 2–7.5 mm/yr and a 5 year interferogram), so it is necessary to make an atmospheric correction to our data before we can expect to extract a tectonic signal.

[15] Several different methods have previously been employed to correct interferograms for atmospheric delays. Stacking N short-baseline and long-timespan interferograms is a common technique [e.g., *Zebker et al.*, 1997; *Williams et al.*, 1998; *Wright et al.*, 2001; *Emardson et al.*, 2003] and can reduce the variance of atmospheric errors by a factor $\sqrt{N}$, but this approach is of limited use if only a few interferograms are available, or if the temporal sampling of SAR acquisitions is uneven.
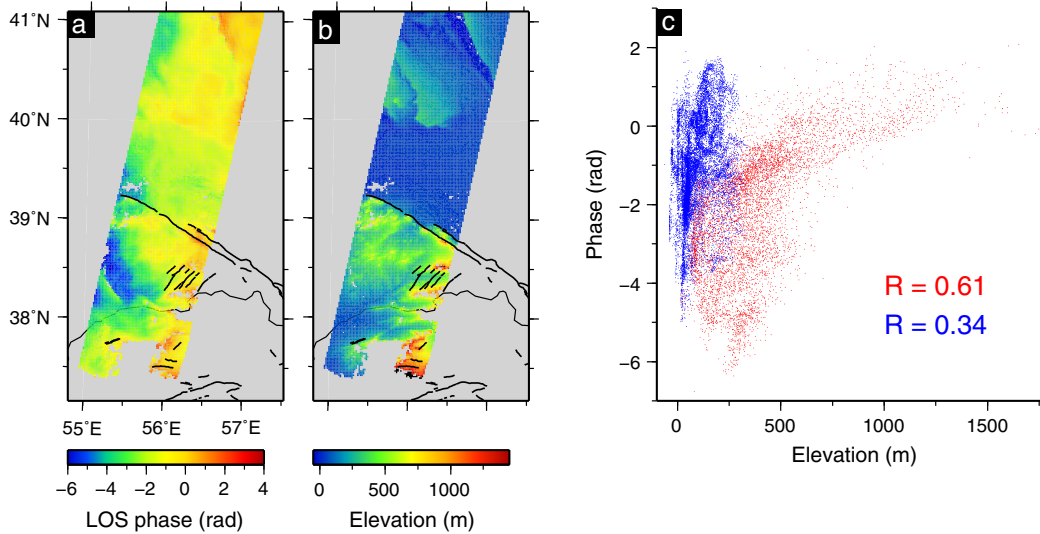
Figure 2. Comparison of interferometric phase and elevation for an example interferogram. (a) LOS phase for interferogram 090513-100811. (b) Elevation for same region as the interferogram, from SRTM. (c) Phase plotted against elevation. Red points are pixels south of the fault, and blue points are pixels north of the fault. *R* values are the correlation coefficients for both subsets of data.

[16] An established empirical method for estimating stratified atmospheric delay is to find the best-fitting linear or exponential relationship between phase and elevation for each interferogram [e.g., *Cavalié et al.*, 2007; *Elliott et al.*, 2008]. However, this method assumes that the same phase/elevation relationship applies across all regions of the interferogram. We found that this was not true for all of our interferograms, with topographically correlated signals often confined to the region south of the Ashkabad fault (e.g., Figure 2). We suggest that this effect is due to the Kopeh Dagh acting as a meteorological barrier to weather systems coming off the Caspian Sea. A similar effect was seen by *Puysségur et al.* [2007], who compared a simple estimate of delay using an empirical phase/elevation relationship as described above to that from a mesoscale weather model for the Lebanese coast. They noted systematic differences between the two estimates of delay over the seaward and landward slopes of Mount Lebanon and suggested that the empirical method could not model stationary meteorological effects. A similar approach can also be applied at multiple scales, to identify and remove components of interferograms that correlate with topography across a variety of lengthscales [*Shirzaei and Bürgmann*, 2012; *Lin et al.*, 2010]. However, all of these methods are susceptible to overcorrection of the data if elevation is correlated with the tectonic signal.

[17] Direct estimates of atmospheric delay can be obtained using GPS [e.g., *Onn and Zebker*, 2006; *Li et al.*, 2006b; *Xu et al.*, 2011] or satellite multispectral data such as MODIS (Moderate Resolution Imaging Spectroradiometer) and MERIS (Medium Resolution Imaging Spectrometer) [e.g., *Li et al.*, 2005, 2006a, 2009]. The use of GPS for this technique is limited to areas with dense station coverage and is not suitable for north-east Iran; we have instead adopted the multispectral method in this study.

[18] Mesoscale or high-resolution atmospheric models have also been used to generate atmospheric delay maps,

either by themselves [*Jolivet et al.*, 2011] or in conjunction with multispectral data [e.g., *Wadge et al.*, 2002; *Puysségur et al.*, 2007]. We will briefly discuss results from using this approach and compare it to the multispectral method in section 6.
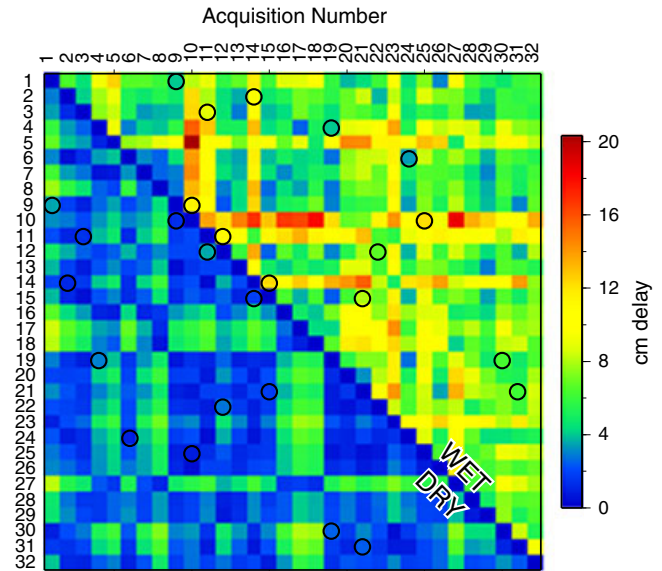
Figure 3. Estimated LOS atmospheric delays based on the ECMWF ERA-Interim numerical weather model, for all potential interferograms on T20d covering the Ashkabad fault. Each colored square represents a potential interferogram, and the color shows the magnitude of the expected atmospheric effects (the range of the delay differences across the interferogram). The wet contribution is shown above the diagonal line, and the hydrostatic or dry contribution is shown below the diagonal line. The 32 acquisition dates are numbered according to Table 1. The black circles show the 13 interferograms we have used in this study.
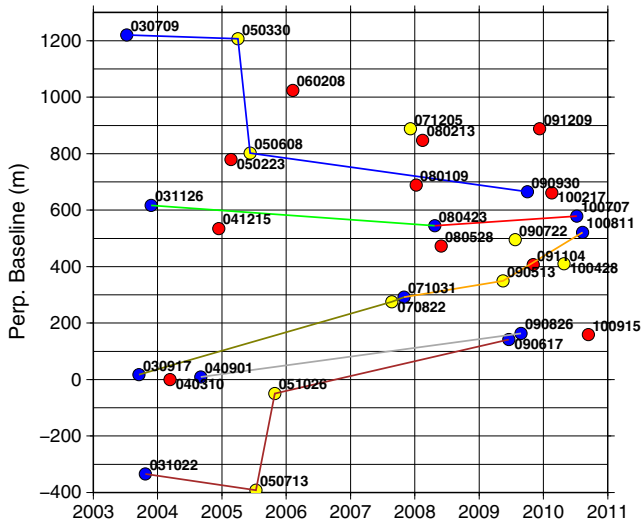
Figure 4. Spatial and temporal baseline plot for Envisat data on T20d covering the Ashkabad fault. Colored nodes represent the 32 satellite acquisitions. Red nodes are mostly (>75%) cloud covered or there are no MERIS data available, yellow nodes are partially cloud covered (75%–20%), and blue nodes are largely cloud-free (<20% cloud). The 13 interferograms that were used in this study are shown as the lines that join pairs of nodes. Note that interferograms are linked together in chains such that only blue cloud-free nodes are located at each end of every chain. Each of the seven chains and subchains have been assigned a different color.

4. Correction of Atmospheric Delay and Construction of Ratemaps

4.1. The MERIS Atmospheric Correction

[19] We use data from the Medium-Resolution Imaging Spectrometer (MERIS) instrument in order to correct our interferograms for atmospheric delay. The MERIS instrument is located on the Envisat satellite and measures reflected solar radiation. We adopt the use of this instrument for our study as MERIS provides a direct estimate of atmospheric water vapor in both stratified and turbulent forms simultaneously with SAR acquisition. We also expect north-east Iran and Turkmenistan to be a good target location to apply this correction technique, as the region generally experiences low cloud cover (mean daily cloud cover is ~40% between 1983 and 2007 from the International Satellite Cloud Climatology Project [*Schiffer and Rossow*, 1983]), which is a major limiting factor in estimating water vapor from MERIS.

[20] The MERIS instrument estimates water vapor from the ratio of radiances in two closely spaced near-infrared spectral channels, one of which lies inside a water absorption region and one of which lies outside. MERIS water vapor retrieval has been validated against GPS zenith delay measurements, and the two estimates were found to agree to 1.1 mm in terms of standard deviations [*Li et al.*, 2006c]. MERIS water vapor estimates have also been shown to closely agree with mesoscale and high-resolution meteorological models [*Puysségur et al.*, 2007; *Zhu et al.*, 2007]. We convert from the MERIS estimate of precipitable water

vapor (PWV) to slant wet delay (SWD, one-way in centimeters) using the equation:

$$SWD = \frac{\Pi \times PWV}{\cos \theta_{inc}} \qquad (1)$$

where θ_{inc} is the local radar incidence angle, and Π is the factor that converts PWV into Zenith Wet Delay. Π depends on temperature but usually varies between 6.0 and 6.5 [*Bevis et al.*, 1992; *Niell et al.*, 2001; *Li et al.*, 2003]; we assume a fixed value of 6.2 for this study [*Li et al.*, 2006c].

[21] Tropospheric pressure differences also make a significant contribution to SAR phase delay [*Elliott et al.*, 2008; *Doin et al.*, 2009]. The absolute delay from this hydrostatic or "dry" part of the atmosphere is greater than the "wet" delay for any single acquisition date, but the wet delay is more variable between dates and so has a greater contribution to radar phase delay in interferograms [*Zebker et al.* 1997]. However, Figure 3 shows that even though the hydrostatic delay is smaller, it is still on the order of several centimeters and so should be corrected. The MERIS instrument estimates surface pressure, but the measurements have been shown to have large associated errors [*Ramon et al.*, 2003]. The MERIS product also contains mean sea level pressures from the ECMWF numerical weather model, and we instead use these to estimate the slant hydrostatic delay (SHD, one-way in centimeters):

$$SHD = \frac{kP_0 \exp(-h/8.34)}{\cos \theta_{inc}} \qquad (2)$$

assuming an exponential decrease in pressure with height above sea level, and a scale height of 8.34 km [*Ramon et al.*, 2003]. Here k is the conversion factor between surface pressure and Zenith Dry Delay, taken to be 0.23 cm/hPa [*Davis et al.*, 1985], P_0 is the pressure at sea level, and h is the surface elevation above sea level, taken from the SRTM DEM.

Table 2. Interferograms Used in This Study Grouped Into "Chains," Timespan Between Acquisitions and Chain Color for Figures 4 and 9[a]

Ifgm Dates (yymmdd–yymmdd)	Timespan (years)	Chain Color	R	g	RMS (cm)
030709–050330	1.7	Blue	0.74	0.99	1.70
050330–050608	0.2				
050608–090930	4.3				
031126–080423	4.4	Green	0.89	0.81	0.59
080423–100707	2.2	Red	0.97	0.99	0.95
030917–070822	3.9	Dark green	0.95	0.95	0.64
070822–071031	0.2				
071031–090513	1.5	Orange	0.59	0.89	0.96
090513–100811	1.2				
040901–090826	5.0	Grey	0.92	1.12	0.72
031022–050713	1.7	Brown	0.60	0.72	1.22
050713–051026	0.3				
051026–090617	3.6				

[a]R is correlation coefficient between interferogram chain and corresponding MERIS correction, g is the gradient of regression line for the two data sets, and RMS is the RMS misfit between the two data sets.
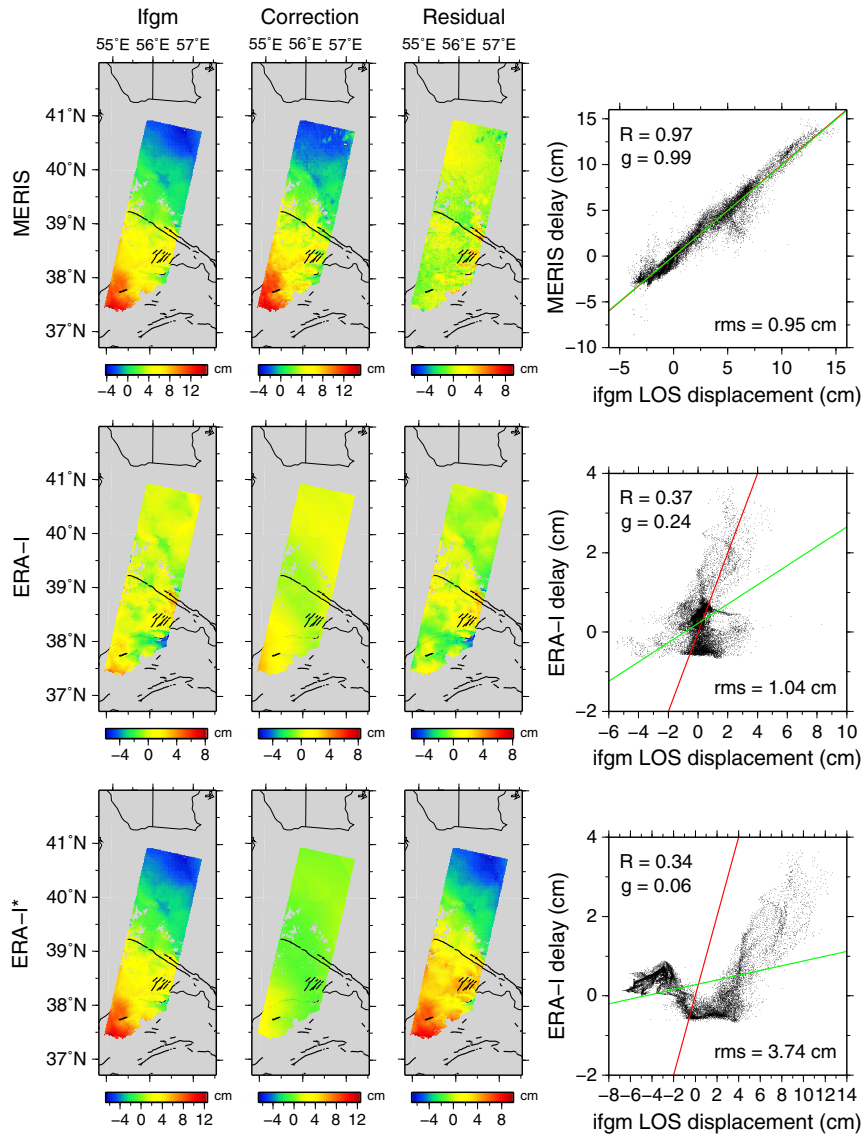
Figure 5. (top row) Example comparison of ∼2 year interferogram (Ifgm, dates 080423–100707) and corresponding atmospheric correction from MERIS radiometry (Correction). An orbital plane and static offset has been added to the interferogram to minimize the residuals between the interferogram and correction. The interferogram and the correction are both shown with the same color scale, in LOS centimeters. A positive LOS displacement corresponds to movement away from the satellite. Residual (Ifgm-Correction) is shown on the right, and individual pixels from Ifgm and Correction are plotted in far-right panel. *g* is gradient of the best fit line shown in green, *R* is the correlation coefficient, and rms is the RMS misfit between the two data sets. Red line (obscured behind green line) is the line of 1:1 correspondence. (middle row) Same as top row, but for ECMWF ERA-Interim atmospheric correction instead of MERIS. (bottom row) Same as middle row, but the orbital plane added to the interferogram is the same as for the top row, and not chosen to minimize the residuals.

[22] Near-IR radiation is reflected by clouds, and this limits the use of MERIS in estimating water vapor to cloud-free regions. Out of the 32 SAR acquisitions covering track 20, 11 are classified as mostly cloud covered (>75% cloud) or there are no data available, 9 are partially cloud covered (20%–75% cloud), and only 12 are largely cloud free (<20% cloud) (see Figure 4 and Table 1).

[23] To interpolate over the data gaps for our largely cloud-free dates, we used the "continuous curvature splines in tension" algorithm from the Generic Mapping Tools package [*Smith and Wessel*, 1990], with a tension of 0.5. However, interpolation over large areas of the mostly or partially cloud-covered water vapor data introduced significant errors on the order of several centimeters LOS delay, and so we decided to only use the largely cloud-free SAR acquisitions. To this end, we stacked 13 interferograms for which the two SAR acquisitions were on cloud-free dates, or formed part of chains of interferograms for which the chain started and ended on cloud-free dates (Figure 4). The atmospheric contribution from any mostly or partially cloud-covered
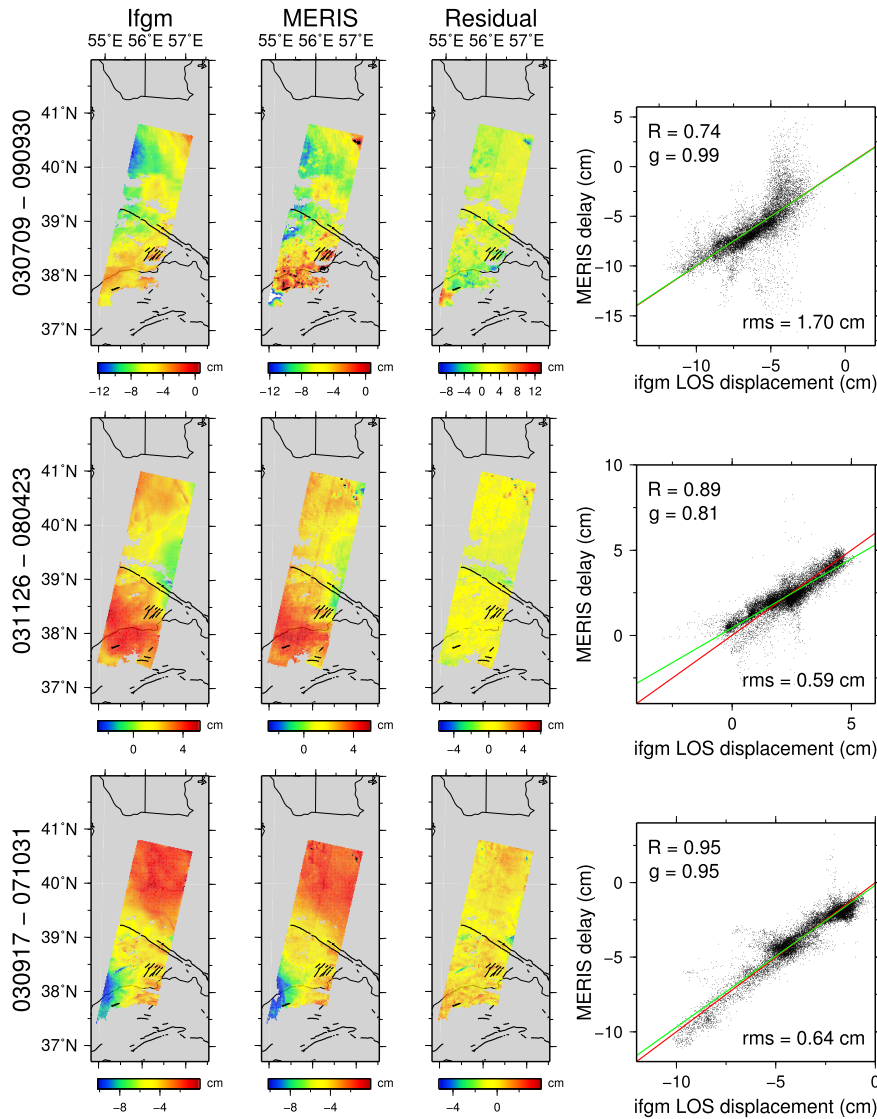
Figure 6. (top row) Interferogram produced from dates 030709–090930 (Ifgm) and corresponding atmospheric correction (MERIS). An orbital plane and static offset has been added to the interferogram to minimize the residuals between the interferogram and MERIS correction. The interferogram and the MERIS correction are both shown with the same color scale, in LOS centimeters. A positive LOS displacement corresponds to movement away from the satellite. Residual (Ifgm-MERIS) is shown on the right, and individual pixels from Ifgm and MERIS correction are plotted in far-right panel. g is gradient of the best fit line shown in green, R is the correlation coefficient, and rms is the RMS misfit between the two data sets. Red line (obscured behind green line) is the line of 1:1 correspondence. (middle row) Same as top row, but for dates 031126–080423. (bottom row) Same as top row, but for dates 030917–071031.

acquisitions in the middle nodes of chains cancel out and do not contribute to the stack.

[24] We compared each chain of interferograms with the combined wet MERIS and hydrostatic ECMWF atmospheric correction (from here on termed "the MERIS correction" for simplicity), also solving for an orbital plane and static offset that minimized the residual between the chain and the correction. For chains of interferograms spanning < 7 years, the expected deformation signal is small compared to the atmospheric signal, so we expect a strong correlation between the chain and the correction if the MERIS correction is correct. For all seven chains, the correlation between

atmospheric correction and chain interferogram was very good (mean correlation coefficient 0.8, range 0.59–0.97), and the mean slope of the regression line between the two was 0.92 with a standard deviation of 0.13. The RMS misfit between MERIS correction and chain interferogram varies from 0.6 to 1.7 cm (Table 2). An example of the comparison between one interferogram chain and the corresponding MERIS correction is shown in the top row of Figure 5 and demonstrates the necessity of correcting for the atmosphere in this region, as the majority of the phase signal comes from atmospheric differences. Similar figures for the other six chain interferograms are shown in Figures 6 and 7.
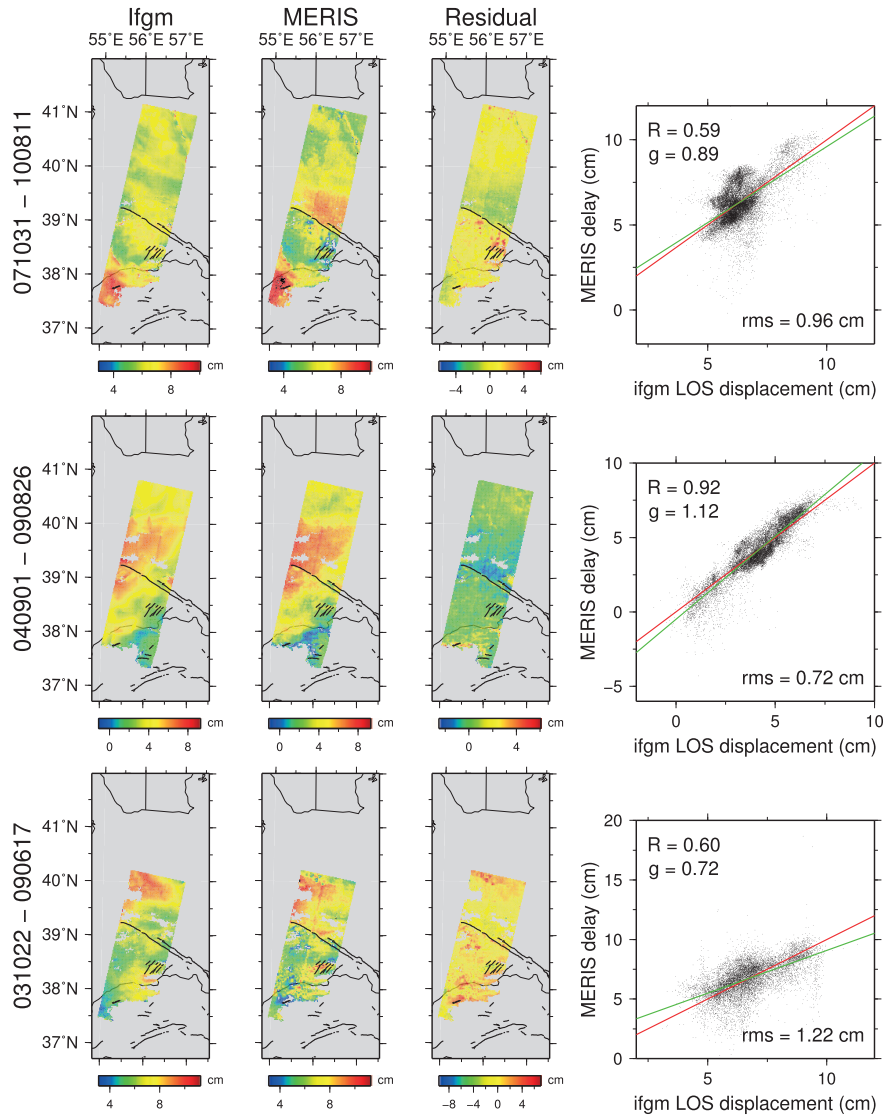
Figure 7. Same as previous figure, but for dates (top) 071031–100811, (middle) 040901–090826, and (bottom) 031022–090617.

4.2. Ratemap Construction

[25] We subtracted the MERIS corrections from each interferogram, then added the phase from all interferograms, and divided by their total timespan to create a ratemap. We used only those pixels which are coherent in all interferograms, and all interferograms were weighted equally. This ratemap still contains a residual orbital error which is the sum of orbital errors from each interferogram. This residual error takes the form of a planar phase gradient across the ratemap over lengthscales of less than ~200 km. To empirically remove this error, we inverted the ratemap for a best-fitting plane and removed this plane from the ratemap. This removes any fault-parallel orbital error but also will remove a linear trend from the interseismic signal in the fault-perpendicular direction. However, we account for this later when we model the interseismic signal by simultaneously solving for a fault-perpendicular linear ramp.

[26] We also repeated the steps above, but without making the atmospheric correction with the MERIS data.

Both the uncorrected and corrected ratemaps are shown in Figure 8.

[27] The uncorrected ratemap does not show the arctan tectonic signal that is characteristic of strike-slip interseismic strain accumulation [*Savage and Burford*, 1973]. The corrected ratemap, however, clearly shows a difference in linear velocity across the Ashkabad fault of ~3 mm/yr LOS, qualitatively consistent with right-lateral slip on the fault.

[28] We next constructed fault-perpendicular profiles across the uncorrected and corrected ratemaps (Figure 8), first downsampling each ratemap to a resolution of 1600 m. All pixels were projected onto the profile line. We calculated a mean profile and 1-sigma bounds for each data set by inverting all the ratemap data within 10 km along-profile bins, weighting the inversion using a variance-covariance matrix to account for spatial correlation between ratemap pixels. The variance-covariance matrix was estimated by fitting a 1-D autocovariance function of the form $\sigma^2 e^{-d/d_c}$
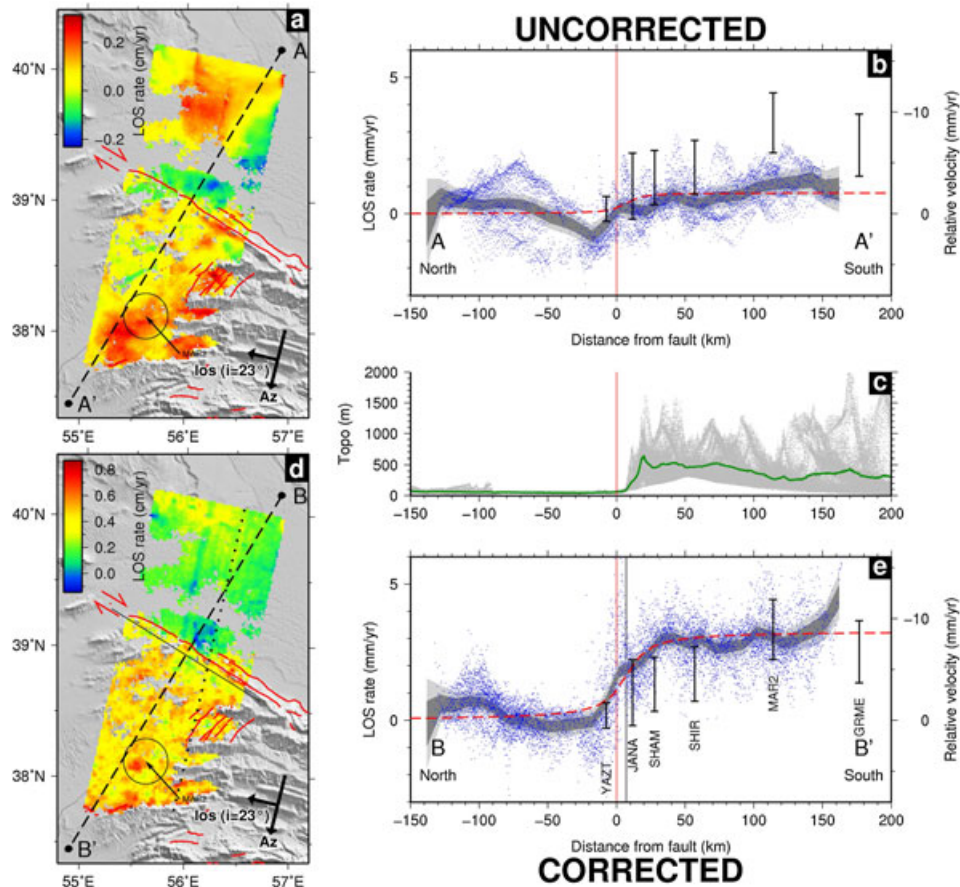
Figure 8. (a) Ratemap for T20d before correction for atmospheric effects. LOS rate is the line-of-sight range rate, and an increase in LOS rate corresponds to an increase in the rate of movement away from the satellite. The perpendicular pairs of arrows show the satellite orbit direction (Az), the satellite line-of-sight direction (los), and the incidence angle (*i*) at the center of the scene. (b) LOS rate profile for T20d. The thick grey bands show the 1- and 2-σ error bounds on LOS rate. Blue points are individual pixels from the ratemap, projected onto the profile line. Black bars are the horizontal GPS velocities and error bounds shown in Figure 1, projected onto the profile line and converted into satellite LOS rates. Velocities predicted by our best fit slip model are plotted as a red dashed line. A static offset has been added to the model line and to the data profiles in order to fix the model line at 0 mm/yr in the far-field north of the fault. (c) Topographic profile for a 100 km-wide swath centered about the line A–A', where grey points are individual pixels from the DEM, and the green line shows mean elevation. (d, e) Same as for Figures 8a and 8b but for ratemap produced from MERIS-corrected interferograms. Black, fault-parallel line in Figure 8d, and black vertical line in Figure 8e show location of best fit shear localization at depth.

to signals in a nondeforming region of the ratemap [e.g., *Hanssen*, 2001], where σ^2 is the maximum variance, d_c is the 1-D *e*-folding distance, and *d* is the distance between pixels. σ^2 and d_c are found to be 0.7 mm^2/yr^2 and 5 km, respectively.

5. Modeling Strain Accumulation

[29] As we only have InSAR data acquired from one look direction, we use the assumption that all displacements are fault-parallel and horizontal. We model the Ashkabad fault as a buried infinite screw dislocation in an elastic half-space, where during the interseismic period, right-lateral aseismic slip occurs at a rate *s* below a locking depth *d*. For a displacement *y* at a perpendicular distance *x* from the fault, $y(x) = (s/\pi) \times \arctan(x/d)$ [*Savage and Burford*, 1973]. We

performed a parameter search over the ranges 0–20 mm/yr for slip rate and 0–25 km for locking depth, at 1 mm/yr and 0.5 km intervals, respectively. For each combination of parameters, we found a static offset in LOS rate and a fault-perpendicular linear trend (to remove any residual fault-perpendicular orbital error) that minimized the total RMS misfit between the model and data profiles. We also noted that the LOS rate profile was asymmetric about the location of the mapped fault, and so we considered that shear localization at depth may be offset from the mapped fault trace at the surface [e.g., *Jolivet et al.*, 2008]. As such, we reran the parameter search 30 times, each time moving the model fault location between ±15 km either side of the mapped fault, in 1 km increments. This enabled us to find the offset which further minimized the RMS misfit of the model to the data.
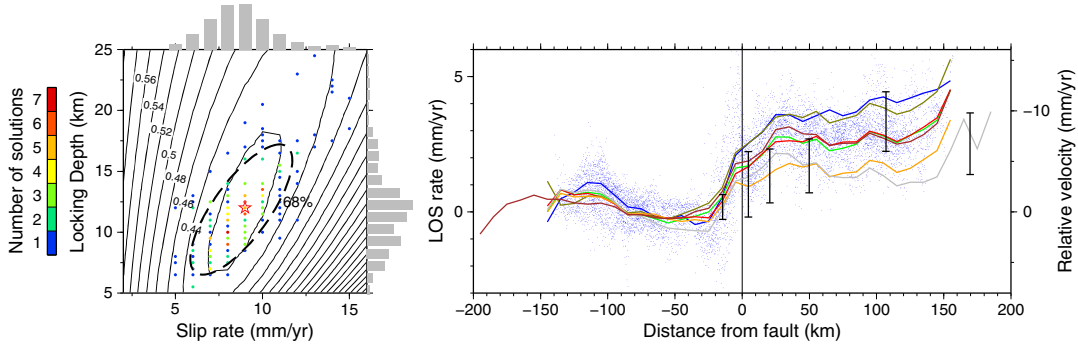
Figure 9. (left) LOS rate profiles showing results of jackknife method of error analysis. Colored lines are the seven mean profile lines resulting from removing each of the seven "interferogram chains" from the stack, where the color corresponds to the chain that has been removed (see Table 2 and Figure 4). Blue points and black GPS bars are the same as for profiles in Figure 8. (right) Solution-space plot for our model showing results of Monte Carlo error analysis. Contours show the RMS misfit in mm/yr for the unperturbed data set. The red star shows our best fit solution. Circles are the best fit parameters for 200 perturbed data sets. If more than one solution is in the same location, the circle is colored accordingly. The distributions of these 200 circles are also shown in histograms for both slip rate and locking depth. The 68% confidence ellipse is shown by the dashed black ellipse.

[30] Our best fit model, corresponding to the minimum of RMS misfit, has a slip rate of 9 mm/yr below a locking depth of 12 km (see Figure 8e), and the shear is localized 7 km to the south-west side of the mapped fault. The 7 km offset of the mapped fault from the shear localization, combined with the 12 km locking depth, implies that the Ashkabad fault dips to the south-west at ∼60°. A southward dipping fault is consistent with the geological cross sections presented by *Lyberis and Manby* [1999], and with the uplifted geomorphology of the southern side of the fault. However, some or all of the asymmetry seen in the LOS profile could also be caused by a rigidity contrast across the fault [e.g., *Jolivet et al.*, 2008]. To test how such a rigidity contrast might affect our results, we inverted the data profile again for slip rate, locking depth, and rigidity ratio K according to the equations:

$$y(x) = \begin{cases} \frac{2Ks}{\pi} \arctan\left(\frac{x-\Delta}{d}\right), & \text{if } x > \Delta \\ \frac{2(1-K)s}{\pi} \arctan\left(\frac{x-\Delta}{d}\right), & \text{if } x < \Delta \end{cases} \quad (3)$$

where Δ is the offset between the fault at the surface and the shear localization at depth. K is equivalent to $\mu_2/(\mu_1 + \mu_2)$, where μ_1 and μ_2 are the shear moduli for the regions north and south of the fault. Setting $\Delta = 0$ gives a slip rate of 8 mm/yr and a locking depth of 9.5 km and requires a very strong rigidity contrast across the fault ($K = 0.08$), with the north side of the fault roughly an order of magnitude more rigid than the south side. Setting $\Delta = -7$ km, so that the offset is the same as for our best fit solution, gives a slip rate of 9 mm/yr and a locking depth of 11.5 km, and a smaller rigidity contrast ($K = 0.46$), with the north side of the fault roughly 15% more rigid than the south side. Including a rigidity contrast in our model gives values for slip rates and locking depths that are within our error bounds (see below), and so is not considered further in what follows.

[31] To assess the robustness of the best fit solution, we employ two separate error analysis techniques: a Monte Carlo and a jackknife approach.

[32] First, we used a Monte Carlo method as one way to estimate error bounds on our best fit model. We perturbed our ratemap 200 times with spatially realistic noise (using the same variance-covariance matrix as used previously to derive the mean profile) [*Biggs et al.*, 2007] and then used the same parameter search on each of these data sets to find the best-fitting model. Using principal component analysis [*Jackson*, 1991], we calculated an ellipse about the mean slip rate and locking depth that contains 68% of the 200 solutions in slip rate/locking depth parameter space. The extents of this ellipse define our range of model values: 6–12 mm/yr slip rate and a locking depth of 6.5–17 km (Figure 9).

[33] For the jackknife approach, we removed each of the seven "interferogram chains" from the stack in turn, creating seven different jackknifed ratemaps. We then calculated the best fit slip rates and locking depths for each of these seven ratemaps to test our solution's sensitivity to the removal of any one interferogram chain. The seven average profile lines for each jackknifed ratemap are plotted in Figure 9 and give a range of 5–11 mm/yr for slip rate and 5.5–13.5 km for locking depth. These ranges are similar to those obtained from the Monte Carlo method, and we take the combined range from both methods as the best estimate of the variability of our fault parameters for the Ashkabad fault: 5–12 mm/yr slip rate and 5.5–17 km locking depth.

[34] We also consider the effects of unmodeled fault-perpendicular or vertical motion on our results. Apart from strike-slip motion, we might expect to observe both fault-perpendicular shortening and uplift of the south of the fault relative to the north side in this region. However, both of these movements would result in interferometric signal of the opposite sense to that which we observe from right-lateral strike-slip faulting and which we see in our ratemap, so we can consider our strike-slip rate estimates as lower bounds.

[35] The eastern edge of our ratemap appears to reflect a small step-over shown in the mapped fault trace, and we investigated the effect of splitting our ratemap into two separate data sets. If we split the data along the track-parallel
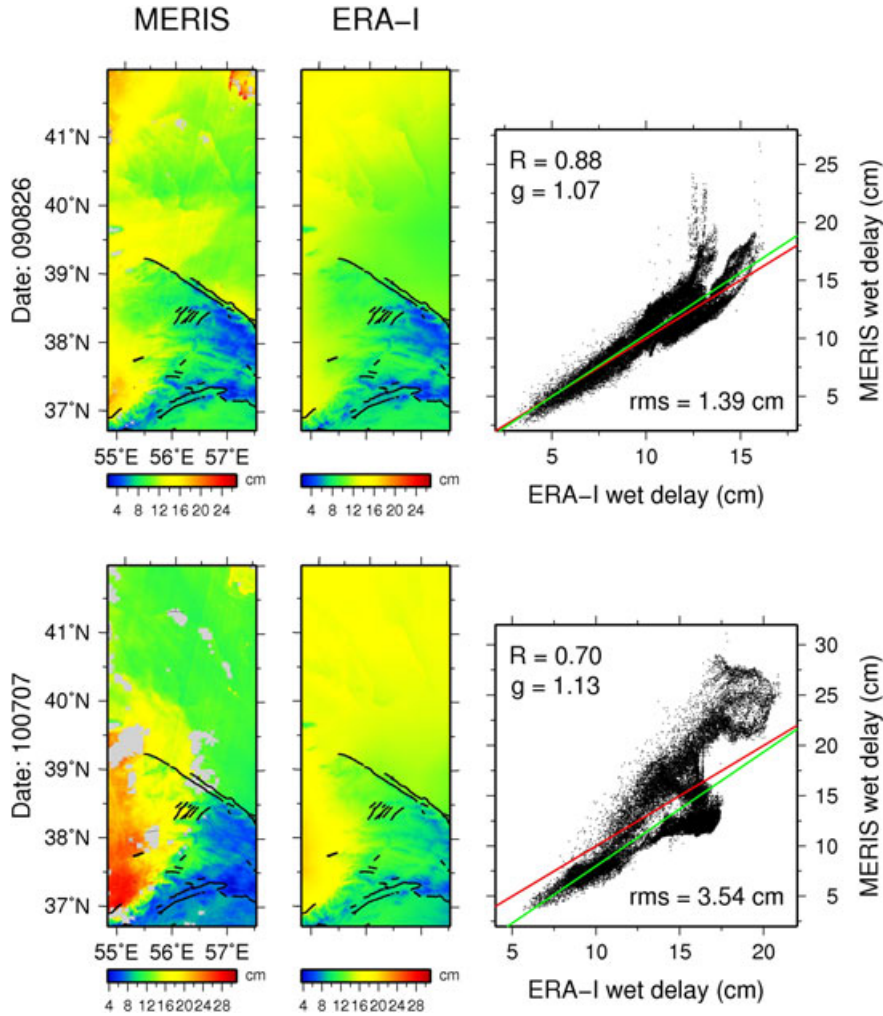
Figure 10. Example comparison of wet delay maps from (left column) MERIS and (middle column) ERA-I for two example acquisition dates (090826 and 100707). Individual pixels from MERIS and ERA-I wet delay maps are plotted in the right column. *g* is gradient of the best fit line shown in green, *R* is the correlation coefficient, and rms is RMS misfit between the two data sets. Red line is the line of 1:1 correspondence. Note that the small region in the NE corner of the two MERIS images with sharp variation in wet delay is coincident with Lake Sarykamysh in Turkmenistan.

dotted line shown in Figure 8d and repeat the modeling procedure outlined above for each data set, we find a best fit slip rate of 8 mm/yr and a locking depth of 6.5 km for the western swath. As for the full swath, we find again that the strain localization at depth is offset from the mapped fault trace by 7 km to the south-west side of the fault. For the eastern swath, we find a best fit slip rate of 10 mm/yr below a locking depth of 8 km, and the strain is localized directly below the northern step-over strand. The best fit values of slip rate and locking depth for both subswaths fall within the error bounds found previously, but the locking depth is smaller for both subswaths, indicating that by ignoring the step-over, we may be overestimating the locking depth in our original estimate. Our results also suggest that while the southernmost strand of the Ashkabad fault is likely to dip to the south-west, the northern strand may be vertical and points to a significant offset in shear localization at depth. However, it is important to note that this inference is based only on a small subswath of data, so is currently tentative.

[36] In order to assess how our results are affected by our inversion method and by uncertainties in the MERIS corrections, we also ran tests on synthetic interferograms. These show that our inversion method can retrieve the true slip rate and locking depth to within ± 3 mm/yr and ± 7 km, respectively, which is similar to the errors estimated using both our jackknife and Monte Carlo approaches. The full synthetic test results are presented in Appendix A.

6. Comparison of Atmospheric Delays From MERIS and ECMWF ERA-Interim

[37] Our results have demonstrated the importance of correcting InSAR data for atmospheric effects, especially when attempting to measure small rates of deformation. However, although we have shown that MERIS data can be used successfully for this task, the MERIS instrument can only be used to correct Envisat SAR scenes that are acquired during the daytime and under largely cloud-free conditions.
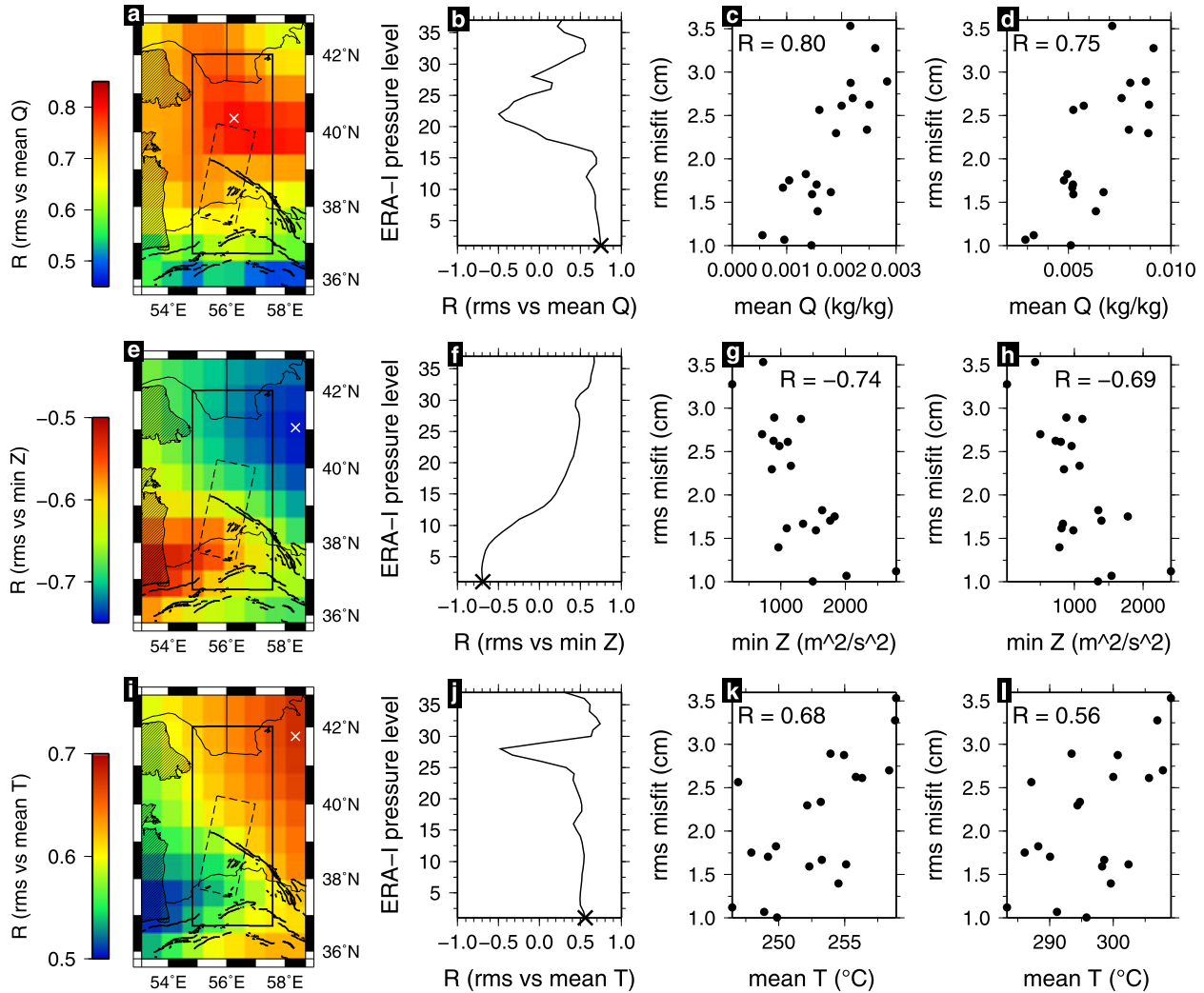
Figure 11. (a) Map showing spatial variability of the correlation between mean Q (relative humidity) and RMS misfit between MERIS and ERA-I wet delay maps. Black box is the region over which RMS misfit is calculated, and dashed box shows location of the track 20 InSAR swath. The white cross marks the location corresponding to the graph in Figure 11c. (b) Map showing variation with height of the correlation between mean Q (relative humidity) at a given level and RMS misfit between MERIS and ERA-I wet delay maps. Pressure level is a rough proxy for height. One is the pressure level roughly around sea level, 37 is the pressure level at around 50 km, and 25 is the pressure level at roughly 15 km. (c) Graph showing correlation between mean Q with height and RMS misfit between MERIS and ERA-I wet delay maps. Each dot represents a separate epoch, and mean Q for each epoch has been calculated over one vertical profile of Q versus height, located at white cross in Figure 11a. (d) Graph showing correlation between mean Q and RMS misfit between MERIS and ERA-I wet delay maps. Each dot represents a separate epoch, and mean Q for each epoch has been calculated over map of Q for the lowest-elevation pressure level. (e–h) Same as for Figures 11a–11d but for minimum Z (geopotential). (i–l) same as for Figures 11a–11d but for mean T (temperature).

There are no plans to mount a similar instrument on any of the upcoming SAR satellites, and it is therefore important that a more general approach is developed to correct radar interferograms for atmospheric delay. Ideally, such a technique could be used under all weather conditions, at any time, for all SAR satellites. One such approach is that taken by *Jolivet et al.* [2011], who used model outputs from the ECMWF ERA-Interim reanalysis model (from here on termed ERA-I) to generate atmospheric delay maps, and who find their technique significantly reduces RMS noise in interferometric phase for a region in north-east Tibet.

6.1. Comparison of MERIS and ERA-I

[38] We previously created delay maps using the method of *Jolivet et al.* [2011] in order to estimate the expected magnitude of atmospheric delays for our data set (shown in Figure 3). We also used these delay maps as an alternative to the MERIS data for correcting atmosphere in interferograms and formed an ERA-I-corrected ratemap using the same method outlined in section 4.2. The ERA-I-corrected ratemap showed no clear tectonic signal across the Ashkabad fault (see Figure S1 in the supporting information). The

hydrostatic component of the MERIS correction is derived from the ERA-I model outputs, so any discrepancy between the two corrections is likely to arise from differences in the estimate of the wet delay component. Therefore, we compared the wet delay maps derived from MERIS and ERA-I for all 21 cloud-free or partially cloudy acquisition dates. We found that there were strong discrepancies between the ERA-I and MERIS-derived wet delay maps for most dates, and the two estimates agreed closely on only a few dates (Figure 10). The RMS misfit between the two data sets for all 21 dates varied between 1 cm and 3.5 cm.

[39] We found a similar pattern when we extended this comparison to pairs of acquisition dates: to chain interferograms and their corresponding ERA-I correction maps. As previously outlined for the MERIS correction maps in section 4.1, we compare each chain interferogram with an ERA-I correction map, also solving for an orbital plane and static offset that minimizes the residual between the two. Six out of seven ERA-I corrections show weak correlations with the chain interferograms (mean correlation coefficient 0.4, range 0.20–0.59), and the two data sets look visually dissimilar. Only one of the seven chain interferograms and its corresponding ERA-I correction shows a strong correlation (correlation coefficient of 0.84).

[40] However, despite this weak correlation, the RMS misfits between ERA-I corrections and chain interfograms are on average only ∼10% larger than the equivalent MERIS-interferogram RMS misfits. We postulate that these low RMS misfits are misleading, as the orbital correction made as part of the comparison appears to be trading off with the atmospheric signal, producing unrealistically low RMS misfit values for the ERA-I correction maps. We therefore assumed that the MERIS atmospheric correction is largely accurate, and then used the MERIS-derived orbital planar adjustment for each chain interferogram, just solving for a static offset to minimize the residuals. In this case, the mean RMS misfit between the chain interferograms and the ERA-I corrections is 1.7 cm, significantly higher than the equivalent value of 1 cm for the MERIS corrections (e.g., see Figure 5).

[41] It is interesting to note that the single ERA-I correction that has the highest correlation coefficient of 0.84 and the lowest RMS misfit of 0.7 cm is formed from two delay maps that both individually showed small RMS misfits (less than 1.5 cm) between the wet delays from ERA-I and MERIS, i.e., the water vapor estimation from the ERA-I model was relatively accurate for both the master and slave dates.

6.2. Prediction of the Quality of ERA-I Water Vapor Retrieval

[42] Since the wet delay comparison between MERIS and ERA-I appears to be the critical factor for when interferogram correction is good or poor, we attempted to find a predictor of the days on which the RMS misfit between ERA-I and MERIS wet delays is large and on which it is small. In the region of interest, we looked for correlations between any of the 16 model output parameters from the ERA-I model (e.g., temperature and humidity) and the RMS misfit between MERIS and ERA-I wet delays, for all 21 cloud-free/partially cloudy acquisition dates. We found significant correlations between MERIS and ERA-I wet delay misfit

and several parameters, and the three strongest correlations were with relative humidity, geopotential, and temperature.

[43] The strongest predictor of MERIS-ERA-I wet delay misfit was the mean of relative humidity. We examined the correlation between the RMS misfit and the mean of relative humidity across a 3-D region of interest (2960 nodes; 37 pressure levels, 8 longitude increments, and 10 latitude increments) but also examined how the correlation changed spatially in the horizontal domain (by calculating the correlation between RMS misfit and mean relative humidity for each of 80 vertical profiles) and how the correlation changed spatially with height (by calculating the correlation between RMS misfit and mean relative humidity for each of 37 pressure levels). The results are shown in Figures 11a–11d. The second strongest correlation was between RMS misfit and minimum geopotential (Figures 11e–11h). Geopotential is proportional to the height of the pressure levels, so minimum geopotential is a proxy for surface pressure. When the minimum geopotential is high, surface pressure is high and vice versa. The third strongest correlation was with mean temperature (Figures 11i–11l).

[44] In terms of horizontal spatial variability, the parameters mean relative humidity, minimum geopotential, and mean temperature were most strongly correlated with RMS misfit to the North of the Kopeh Dagh, in the Turkmen Basin. The correlation is positive with mean relative humidity and with mean temperature, indicating that the ERA-I model has good water vapor estimation when both relative humidity and temperature are low. The correlation with minimum geopotential is negative, indicating that the ERA-I model has good water vapor estimation when surface pressure is high.

7. Tectonic Discussion

[45] Our InSAR measurements show that the Ashkabad fault is accumulating strain at a rate of 5–12 mm/yr below a locking depth of 5.5–17 km. This estimate is at the western end of the Kopeh Dagh and so reflects motion of the South Caspian Block relative to Eurasia.

[46] Our locking depth of 5.5–17 km is relatively shallow but is consistent with the <15 km depths of earthquakes in the Kopeh Dagh [*Jackson et al.*, 2002].

[47] Unpublished GPS data from a PhD Thesis [*Tavakoli*, 2007] suggest a slip rate of around 9 mm/yr for the Ashkabad Fault, supporting our best fit slip rate. *Mousavi et al.* in review have recently refined this data set and reduced the errors on several stations, refining the GPS slip rate to 6–7 mm/yr. An earlier GPS estimate of slip rate on the Ashkabad fault is 2–4 mm/yr [*Masson et al.*, 2007], based on the motion of station SHIR relative to Eurasia (Figure 1). However, we suggest that this low value arises as SHIR is in the central, deforming portion of the Kopeh Dagh, and is therefore not representative of South Caspian motion.

[48] *Lyberis and Manby* [1999] suggested a 37.5 km cumulative right-lateral offset across the western Kopeh Dagh since the Miocene-Pliocene boundary, yielding a slip rate for the Ashkabad fault of 6.5–7.5 mm/yr (assuming all the strain is localized onto the Ashkabad fault). The offset is based upon an estimate of 75 km N-S shortening across the Kopeh Dagh from restoring a balanced cross section, and partitioning this shortening into range-parallel and

range-perpendicular components. A similar total offset is found by *Hollingsworth et al.* [2008], who measure a maximum of 35 km dextral displacement of folded Cretaceous and Neogene sediments across the Ashkabad fault near the town of Bakharden (B in Figure 1).

[49] *Trifonov* [1978] identified a right-lateral displacement of a qanat (underground irrigation tunnel) and river bank by 10 m, at a site that is located in the region covered by our InSAR swath. However, they do not date the offset feature, only claiming that the earliest such qanat lines were constructed before 500 B.C. The oldest known qanats in Iran are around 3000 years old [*Javan et al.*, 2006], and this age yields a rough lower bound on slip rate of ∼3 mm/yr. Our slip rate of 5–12 mm/yr would imply an age of 2000–800 years for this qanat line. From similar studies of other qanat tunnels across the Ashkabad fault, *Trifonov* [1971] inferred an average slip rate of 3–8 mm/yr.

[50] *Copley and Jackson* [2006] revised the plate circuit closure models of *Jackson et al.* [2002] for northern Iran and the South Caspian, and argue for relatively fast South Caspian-Eurasia motion. Their results imply that the slip rate on the western Ashkabad fault could be 7–11 mm/yr, if all the strain were localized on one fault. This model is consistent with the tectonics of the Talesh and Alborz, but this model may not be valid as the plate circuit is closed over a large area, and assumes no rotation of the South Caspian relative to its surroundings.

[51] *Djamour et al.* [2010] present a different view of South Caspian motion, based on several GPS vectors located just north of the Alborz, along the southern shore of the South Caspian. They use an elastic block model and find an Euler pole for the South Caspian Block in central Turkmenistan, producing a strong clockwise rotation of the South Caspian, in contrast to the pure translation suggested by *Copley and Jackson* [2006]. This block model predicts a slip rate on the western Ashkabad fault of ∼3 mm/yr. This block model is also consistent with the tectonics of the Talesh and Alborz. However, in this model, all GPS sites are very close to the active thrust faults within the Alborz. Also, the block model is defined by only six sites, one of which is the station SHIR, which may not be representative of South Caspian motion.

[52] Therefore, our slip rate estimate is consistent with geological and geomorphological results from *Lyberis and Manby* [1999] and *Trifonov* [1978], and with the geodetic results of *Tavakoli* [2007] and *Mousavi et al.* in review. Our estimate also fits into the model of South Caspian motion suggested by *Copley and Jackson* [2006] and *Jackson et al.* [2002]. However, our estimate is incompatible with the earlier GPS measurements of *Masson et al.* [2007] and suggests that the slip rate is 1.25–6 times faster. Our results are also in disagreement with the regional block model of *Djamour et al.* [2010] and support a relatively fast moving South Caspian Block, with little rotation.

[53] If all of the accumulated strain across the Ashkabad fault is released seismically, then our results suggest that the recurrence interval of a large earthquake on the Ashkabad fault is 1.25–6 times shorter than is suggested by the results of *Masson et al.* [2007]. With a locking depth of 12 km, a fault dip of 60° and a slip rate of 5–12 mm/yr, and assuming a slip-to-length ratio of 3×10^{-5} and a shear modulus of 3×10^{10} Pa, the strain necessary for a M_w 7

earthquake on this section of the fault will be generated every 140–340 years.

8. Conclusions

[54] Our InSAR data have demonstrated that the western Ashkabad fault has a slip rate of 5–12 mm/yr, significantly faster than previous geodetic estimates. *Molnar and Dayem* [2010] found that most major strike-slip faults worldwide (those with slip rates greater than 10 mm/yr) are bounded by regions of strong lithosphere on at least one side, and suggest that this is due to the concentration of strain near the boundaries of strong regions immersed in a deforming medium. As the Ashkabad fault is likely to represent a contrast in lithospheric strength, it therefore might be expected that strain should be concentrated along the fault, and this is supported by our measurement of relatively rapid strain accumulation across the fault. Our fast slip rate for the Ashkabad fault also raises the hazard the fault represents to local populations in Turkmenistan and north-east Iran, and particularly to Ashkabad City.

[55] We have also shown the importance of correcting for atmospheric effects in InSAR. The atmospheric signal is significantly larger than the tectonic signal in our interferograms and atmospheric correction with MERIS data was essential in order to retrieve tectonic strain across the Ashkabad fault. We have attempted to validate the use of ERA-I numerical model outputs for atmospheric correction and find that this technique does not work satisfactorily for this region when compared to the independent MERIS estimate. The ERA-I model does not satisfactorily retrieve atmospheric water vapor content in this region under warm, low pressure and high humidity conditions. This is likely due to the close proximity of the Caspian Sea and highly variable weather systems which are not well-modeled by ERA-I.

Appendix A: Synthetic Tests

[56] In order to assess the robustness of our inversion method and to explicitly assess how uncertainties in the MERIS corrections affect our results, we ran tests on synthetic interferograms. The synthetic interferograms were generated and used as follows:

[57] For direct comparison with our data, we generated sets of 13 synthetic interferograms that correspond to the 13 real interferograms used in this study (see Figure 4), constructed from the same 18 acquisition dates.

[58] We first generated orbital errors for each of the 18 acquisition dates. From the network inversions of hundreds of interferograms, empirical estimates of the distribution of orbital errors have been made for Envisat and ERS acquisitions by several authors [e.g., *Biggs et al.*, 2007; *Elliott*, 2009; *Wang et al.*, 2009]. These studies all find that if the orbital errors are treated as planar, the planar coefficients are roughly normally distributed about zero, with 1σ values of the order of ∼0.4 mm/km in the E-W direction and ∼0.2 mm/km in the N-S direction. However, we also considered that the orbital errors contain a quadratic component of the form $ax^2 + by^2 + cxy + dx + ey$. To estimate the distributions of these coefficients, we use unpublished results from analysis of the $72 \sim 400$ km long Envisat interferograms over northern Tibet presented in
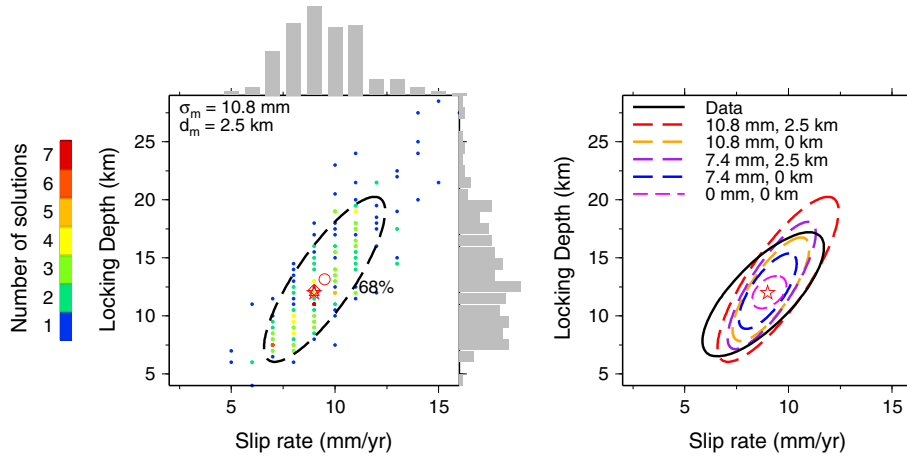
Figure A1. (left) Solution-space plot for our model showing results of synthetic tests. The red star shows the input model of 9 mm/yr slip rate and 12 km locking depth. Colored dots are the best fit parameters for 200 sets of synthetic interferograms, generated from the same tectonic signal and coherence mask combined with randomized atmospheric and orbital components. If more than one solution is in the same location, the circle is colored accordingly. The distribution of these 200 estimates is also shown in histograms for both slip rate and locking depth. The 68% confidence ellipse is shown by the dashed black ellipse. The red circle is the mean of the 200 solutions, and the red triangle and red diamond (which plot on top of the red star) are the mode and median of the 200 solutions. MERIS atmospheric delays are assumed to have a σ_m of 10.8 mm, and a d_m value of 2.5 km. (right) Comparison between 68% confidence ellipses from synthetic tests run with various combinations of σ_m and d_m values. Ellipse labeled data is the 68% confidence ellipse from the error analysis of the real data, shown in Figure 9.

Elliott [2009]. Using these results, for each acquisition date, we draw values for the coefficients *a*, *b*, *c*, *d*, and *e* randomly from unbiased normal distributions with 1σ values of 3×10^{-3} mm/km², 8×10^{-3} mm/km², 4×10^{-3} mm/km², 0.40 mm/km, and 0.21 mm/km, respectively.

[59] To simulate uncertainties on the MERIS corrections, we perturb the MERIS corrections for each of the 18 acquisition dates. This is done using a 1-D covariance function that varies with distance *d* between pixels as $\sigma_m^2 e^{-d/d_m}$, where σ_m is the uncertainty for the MERIS water vapor retrievals, and d_m is the *e*-folding distance that takes into account spatial correlation of these uncertainties between pixels. *Li et al.* [2006c] validate MERIS data over Germany for all seasons between latitudes 48°N to 55°N and find that the RMS of the difference in PWV values between MERIS and GPS measurements is 1.1 mm, which corresponds to $\sigma_m = 7.4$ mm of atmospheric delay in the satellite LOS. Water vapor retrieval by the MERIS instrument is performed on a pixel-by-pixel basis [*Fischer and Bennartz*, 1997], and it is therefore commonly assumed that uncertainties are uncorrelated between pixels, corresponding to a d_m value of zero. However, we also consider that both of these values for σ_m and d_m may be underestimates. For σ_m, we also try using the 1.6 mm theoretical accuracy of MERIS PWV retrieval [*Bennartz and Fischer*, 2001], which corresponds to a $\sigma_m = 10.8$ mm uncertainty in LOS delay. For d_m, we consider the possibility that errors are correlated between neighboring pixels, and we use a d_m value of 2.5 km, which would allow correlation of errors between several neighboring ~1.2 km MERIS pixels. We also take into account the effects of errors in our assumed conversion factor Π of 6.2, since Π varies as a function of surface temperature [*Bevis et al.*, 1992, 1994]. We calculate mean surface temperatures from ECMWF ERA-I model

solutions over the region 37.5°N–40.5°N, 55°E–57°E for each of the 18 acquisition dates. These temperatures vary between 9.7°C–36.7°C, which corresponds to a range in Π of 6.4–6. Therefore, by using a fixed value of 6.2, we introduce a maximum error for any one MERIS correction of ~3.2%. To simulate the effect of choosing a static value for Π, each perturbed MERIS correction is linearly scaled by a random value between 0.968 and 1.032.

[60] Differences in orbital errors and MERIS corrections are then calculated for each of the 13 synthetic interferograms.

[61] The tectonic signal is calculated for each of the 13 interferograms, assuming a known slip rate and locking depth, and based on the timespan of each interferogram. To generate the tectonic signal, we use a back slip model where slip occurs at the imposed rate on a vertical fault below the specified locking depth, and is calculated using the Okada formulation for shear faulting in an elastic half-space [*Okada*, 1985]. In this case, we used 9 mm/yr and 12 km for slip rate and locking depth, corresponding to our best fit model from section 5.

Table A1. Mean and Half-Width of 68% Error Ellipse in Slip Rate/Locking Depth Parameter Space, for Various Combinations of σ_m and d_m MERIS Uncertainties[a]

	$\sigma_m = 0$ mm	$\sigma_m = 7.4$ mm	$\sigma_m = 10.8$ mm
$d_m = 0$ km	9.1 ± 0.8 mm/yr 12.0 ± 1.4 km	9.0 ± 1.4 mm/yr 12.1 ± 3.2 km	9.2 ± 1.9 mm/yr 12.3 ± 4.5 km
$d_m = 2.5$ km	N/A	9.2 ± 2.1 mm/yr 12.6 ± 5.5 km	9.5 ± 2.9 mm/yr 13.1 ± 7.1 km

[a]Input slip rate and locking depth are 9 mm/yr and 12 km, respectively.

[62] The coherence mask of our real ratemap is applied to each interferogram. While in reality each interferogram would have a different coherence mask, pixels are only used if they are coherent in all interferograms, and our inversion and orbital corrections only operate on the ratemap, not individual interferograms, so this choice will not affect any of our results.

[63] Each of the 13 synthetic interferograms is created by summing together the orbital, atmospheric, and tectonic contributions and then applying the coherence mask.

[64] The set of synthetic interferograms are then run through our ratemap construction and inversion method as described in sections 4.2 and 5, including correcting the interferograms for atmospheric effects by removing the unperturbed MERIS corrections. The output is a best fit solution with an estimate of slip rate and locking depth.

[65] This process is repeated 200 times, with different perturbed MERIS corrections and different orbital errors used each time. We plot each of the 200 best fit solutions in slip rate/locking depth parameter space and use principal component analysis to calculate the ellipse about the mean slip rate and locking depth that contains 68% of the 200 solutions. We use the extents of this ellipse to define how well we recover the true slip rate and locking depth. To investigate the effect of the MERIS uncertainties on our ability to recover the input model, this experiment was run 5 times, each with varying values used for σ_m and d_m (see Figure A1, right panel, and Table A1).

[66] The results of our tests using our most conservative estimates of MERIS uncertainty ($\sigma_m = 10.8$ mm and $d_m = 2.5$ km) are shown in the left panel of Figure A1. These show that our inversion method can retrieve the true slip rate and locking depth to within ± 3 mm/yr and ± 7 km, respectively, which is similar to the errors estimated using both our jackknife and Monte Carlo approaches (Figure 9).

[67] If either or both of the σ_m and d_m values are chosen to be smaller, there is a corresponding decrease in the uncertainty to which we can recover the input model (Figure A1, right panel, and Table A1). We also note that if uncertainty on MERIS data is not taken into account (i.e., $\sigma_m = d_m = 0$), then our inversion method can recover the true model to within 1 mm/yr slip rate and 1.5 km locking depth. This is indicative of the combined effects on our results of our orbital correction method, the coherence mask, our choice of a static Π value, and our inversion method. It therefore seems that the largest error is introduced by uncertainties in the MERIS measurements.

[68] We also note a slight positive bias in slip rate and locking depth of less than 1 mm/yr and less than 1.5 km for all combinations of σ_m and d_m values (Table A1). This is likely due to the tradeoff between slip rate and locking depth, and the hard limit of zero kilometers locking depth. If the input model has a locking depth close to this limit, then the distribution of any extreme outliers will necessarily be skewed toward large values, which will also lead to a positive skewed distribution for slip rates. However, this bias is small compared to the uncertainties in our results.

References

Baby, H. B., P. Gole, and J. Lavergnat (1988), A model for the tropospheric excess path length of radio waves from surface meteorological measurements, *Radio Sci.*, 23, 1023–1038, doi:10.1029/RS023i006p01023.

Bennartz, R., and J. Fischer (2001), Retrieval of columnar water vapour over land from backscattered solar radiation using the Medium Resolution Imaging Spectrometer, *Remote Sens. Environ.*, 78, 247–283, doi:10.1016/S0034-4257(01)00218-8.

Bevis, M., S. Businger, T. A. Herring, C. Rocken, R. A. Anthes, and R. H. Ware (1992), GPS meteorology: Remote sensing of atmospheric water vapor using the global positioning system, *J. Geophys. Res.*, 97, 15,787–15,801.

Bevis, M., S. Businger, S. Chiswell, T. A. Herring, R. A. Anthes, C. Rocken, and R. H. Ware (1994), GPS meteorology: Mapping zenith wet delays onto precipitable water, *J. Appl. Meteorol.*, 33, 379–386, doi:10.1175/1520-0450(1994)033<0379:GMMZWD>2.0.CO;2.

Biggs, J., T. Wright, Z. Lu, and B. Parsons (2007), Multi-interferogram method for measuring interseismic deformation: Denali fault, Alaska, *Geophys. J. Int.*, 170(3), 1165–1179, doi:10.1111/j.1365-246X.2007.03415.x.

Cavalié, O., M.-P. Doin, C. Lasserre, and P. Briole (2007), Ground motion measurement in the Lake Mead area, Nevada, by differential synthetic aperture radar interferometry time series analysis: Probing the lithosphere rheological structure, *J. Geophys. Res.*, 112, B03403, doi:10.1029/2006JB004344.

Copley, A., and J. Jackson (2006), Active tectonics of the Turkish-Iranian Plateau, *Tectonics*, 25, TC6006, doi:10.1029/2005TC001906.

Davis, J. L., T. A. Herring, I. I. Shapiro, A. E. E. Rogers, and G. Elgered (1985), Geodesy by radio interferometry—Effects of atmospheric modeling errors on estimates of baseline length, *Radio Sci.*, 20, 1593–1607, doi:10.1029/RS020i006p01593.

Dee, D. P., et al. (2011), The ERA-Interim reanalysis: Configuration and performance of the data assimilation system, *Q. J. R. Meteorol. Soc.*, 137, 553–597, doi:10.1002/qj.828.

Djamour, Y., et al. (2010), GPS and gravity constraints on continental deformation in the Alborz mountain range, Iran, *Geophys. J. Int.*, 183, 1287–1301, doi:10.1111/j.1365-246X.2010.04811.x.

Doin, M.-P., C. Lasserre, G. Peltzer, O. Cavalié, and C. Doubre (2009), Corrections of stratified tropospheric delays in SAR interferometry: Validation with global atmospheric models, *J. Appl. Geophys.*, 69, 35–50, doi:10.1016/j.jappgeo.2009.03.010.

Ekström, M., G. Nettles, and A. M. Dziewoński (2012), The global CMT project 2004–2010: Centroid-moment tensors for 13,017 earthquakes, *Phys. Earth Planet. Inter.*, 200–201(0), 1–9, doi:10.1016/j.pepi.2012.04.002.

Elliott, J. R. (2009), Strain accumulation and release on the Tibetan Plateau measured using InSAR, PhD thesis, Univ. of Oxford, Oxford, U. K.

Elliott, J. R., J. Biggs, B. Parsons, and T. J. Wright (2008), InSAR slip rate determination on the Altyn Tagh Fault, N. Tibet, in the presence of topographically correlated atmospheric delays, *Geophys. Res. Lett.*, 35, L12309, doi:10.1029/2008GL033659.

Emardson, T. R., M. Simons, and F. H. Webb (2003), Neutral atmospheric delay in interferometric synthetic aperture radar applications: Statistical description and mitigation, *J. Geophys. Res.*, 108(B5), 2231, doi:10.1029/2002JB001781.

Farr, T., et al. (2007), Shuttle radar topography mission, *Rev. Geophys.*, 45, RG2004, doi:10.1029/2005RG000183.

Fischer, J., and R. Bennartz, (1997), Retrieval of total water vapour content from MERIS measurements, Algorithm Theoretical Basis Document (ATBD), 5, *ESA Ref. PO-TN-MEL-GS-0005*, Eur. Space Res. and Techol. Cent., Eur. Space Agency, Noordwijk, Netherlands.

Goldstein, R. M., and C. L. Werner (1998), Radar interferogram filtering for geophysical applications, *Geophys. Res. Lett.*, 25, 4035–4038, doi:10.1029/1998GL900033.

Hanssen, R. F. (2001), *Radar Interferometry: Data Interpretation and Analysis*, Kluwer Acad., Norwell, Mass.

Hollingsworth, J., J. Jackson, R. Walker, M. Reza Gheitanchi, and M. Javad Bolourchi (2006), Strike-slip faulting, rotation, and along-strike elongation in the Kopeh Dagh mountains, NE Iran, *Geophys. J. Int.*, 166, 1161–1177, doi:10.1111/j.1365-246X.2006.02983.x.

Hollingsworth, J., J. Jackson, R. Walker, and H. Nazari (2008), Extrusion tectonics and subduction in the eastern South Caspian region since 10 Ma, *Geology*, *36*(10), 763–766, doi:10.1130/G25008A.1.

Jackson, J., and D. McKenzie (1984), Active tectonics of the Alpine-Himalayan Belt between western Turkey and Pakistan, *Geophys. J. Int.*, *77*, 185–264, doi:10.1111/j.1365-246X.1984.tb01931.x.

Jackson, J., K. Priestley, M. Allen, and M. Berberian (2002), Active tectonics of the South Caspian Basin, *Geophys. J. Int.*, *148*, 214–245, doi:10.1046/j.1365-246X.2002.01588.x.

Jackson, J. E. (1991), *A User's Guide to Principal Components*, vol. 244, Wiley-Interscience, New York.

Javan, M., A. M. Hassanli, and M. A. Shahrokhnia (2006), The ancient qanats of Iran, in *Proceedings 1st IWA International Symposium on Water and Wastewater Technologies in Ancient Civilizations, National Agricultural Research Foundation, Iraklio (Greece), 28–30 October 2006*, edited by Angelakis, A. D., and D. Koutsoyiannis, pp. 531–534.

Jolivet, R., R. Cattin, N. Chamot-Rooke, C. Lasserre, and G. Peltzer (2008), Thin-plate modeling of interseismic deformation and asymmetry across the Altyn Tagh fault zone, *Geophys. Res. Lett.*, *35*, L02309, doi:10.1029/2007GL031511.

Jolivet, R., R. Grandin, C. Lasserre, M.-P. Doin, and G. Peltzer (2011), Systematic InSAR tropospheric phase delay corrections from global meteorological reanalysis data, *Geophys. Res. Lett.*, *38*, L17311, doi:10.1029/2011GL048757.

Li, Z., J.-P. Muller, and P. Cross (2003), Comparison of precipitable water vapor derived from radiosonde, GPS, and Moderate-Resolution Imaging Spectroradiometer measurements, *J. Geophys. Res.*, *108*(D20), 4651, doi:10.1029/2003JD003372.

Li, Z., J.-P. Muller, P. Cross, and E. J. Fielding (2005), Interferometric synthetic aperture radar (InSAR) atmospheric correction: GPS, Moderate Resolution Imaging Spectroradiometer (MODIS), and InSAR integration, *J. Geophys. Res.*, *110*, B03410, doi:10.1029/2004JB003446.

Li, Z., E. J. Fielding, P. Cross, and J.-P. Muller (2006a), Interferometric synthetic aperture radar atmospheric correction: Medium Resolution Imaging Spectrometer and Advanced Synthetic Aperture Radar integration, *Geophys. Res. Lett.*, *33*, L06816, doi:10.1029/2005GL025299.

Li, Z., E. J. Fielding, P. Cross, and J.-P. Muller (2006b), Interferometric synthetic aperture radar atmospheric correction: GPS topography-dependent turbulence model, *J. Geophys. Res.*, *111*, B02404, doi:10.1029/2005JB003711.

Li, Z., J. P. Muller, P. Cross, P. Albert, J. Fischer, and R. Bennartz (2006c), Assessment of the potential of MERIS near infrared water vapour products to correct ASAR interferometric measurements, *Int. J. Remote Sens.*, *27*, 349–365, doi:10.1080/01431160500307342.

Li, Z., E. J. Fielding, P. Cross, and R. Preusker (2009), Advanced InSAR atmospheric correction: MERIS/MODIS combination and stacked water vapour models, *Int. J. Remote. Sens.*, *30*, 3343–3363, doi:10.1080/01431160802562172.

Lin, Y.-n. N., M. Simons, E. A. Hetland, P. Muse, and C. DiCaprio (2010), A multiscale approach to estimating topographically correlated propagation delays in radar interferograms, *Geochem. Geophys. Geosyst.*, *11*, Q09002, doi:10.1029/2010GC003228.

Lyberis, N., and G. Manby (1999), Oblique to orthogonal convergence across the Turan Block in the post-Miocene, *AAPG Bull.*, *83*, 1135–1160.

Masson, F., M. Anvari, Y. Djamour, A. Walpersdorf, F. Tavakoli, M. Daignières, H. Nankali, and S. van Gorp (2007), Large-scale velocity field and strain tensor in Iran inferred from GPS measurements: New insight for the present-day deformation pattern within NE Iran, *Geophys. J. Int.*, *170*, 436–440, doi:10.1111/j.1365-246X.2007.03477.x.

Massonnet, D., and K. L. Feigl (1998), Radar interferometry and its application to changes in the Earth's surface, *Rev. Geophys.*, *36*, 441–500, doi:10.1029/97RG03139.

McKenzie, D. (1972), Active tectonics of the Mediterranean region, *Geophys. J. Int.*, *30*, 109–185, doi:10.1111/j.1365-246X.1972.tb02351.x.

Molnar, P., and K. E. Dayem (2010), Major intracontinental strike-slip faults and contrasts in lithospheric strength, *Geosphere*, *6*(4), 444–467, doi:10.1130/GES00519.1.

Niell, A. E., A. J. Coster, F. S. Solheim, V. B. Mendes, P. C. Toor, R. B. Langley, and C. A. Upham (2001), Comparison of measurements of atmospheric wet delay by radiosonde, water vapor radiometer, GPS, and VLBI, *J. Appl. Meteorol.*, *18*, 830, doi:10.1175/1520-0426(2001)018<0830:COMOAW>2.0.CO;2.

Okada, Y. (1985), Surface deformation due to shear and tensile faults in a half-space, *Bull. Seismol. Soc. Am.*, *75*(4), 1135–1154.

Onn, F., and H. A. Zebker (2006), Correction for interferometric synthetic aperture radar atmospheric phase artifacts using time series of zenith wet delay observations from a GPS network, *J. Geophys. Res.*, *111*, B09102, doi:10.1029/2005JB004012.

Puysségur, B., R. Michel, and J.-P. Avouac (2007), Tropospheric phase delay in interferometric synthetic aperture radar estimated from meteorological model and multispectral imagery, *J. Geophys. Res.*, *112*, B05419, doi:10.1029/2006JB004352.

Ramon, D., L. Cazier, and R. Santer (2003), The surface pressure retrieval in the MERIS O_2 absorption: Validation and potential improvements, in *IEEE International Geoscience and Remote Sensing Symposium, 2003. IGARSS '03. Proceedings*, vol. 5., pp. 3126–3128, Inst. of Electr. and Electron. Eng., doi:10.1109/IGARSS.2003.1294704.

Rosen, P. A., S. Hensley, G. Peltzer, and M. Simons (2004), Update repeat orbit interferometry package released, *Eos Trans. AGU*, *85*, 47–47, doi:10.1029/2004EO050004.

Savage, J. C., and R. O. Burford (1973), Geodetic determination of relative plate motion in central California, *J. Geophys. Res.*, *78*, 832–845, doi:10.1029/JB078i005p00832.

Schiffer, R. A., and W. B. Rossow (1983), The International Satellite Cloud Climatology Project (ISCCP)—The first project of the World Climate Research Programme, *Bull. Am. Meteorol. Soc.*, *64*, 779–784.

Shabanian, E., O. Bellier, L. Siame, N. Arnaud, M. R. Abbassi, and J.-J. Cochemé (2009), New tectonic configuration in NE Iran: Active strike-slip faulting between the Kopeh Dagh and Binalud mountains, *Tectonics*, *28*, TC5002, doi:10.1029/2008TC002444.

Shirzaei, M., and R. Bürgmann (2012), Topography correlated atmospheric delay correction in radar interferometry using wavelet transforms, *Geophys. Res. Lett.*, *39*, L01305, doi:10.1029/2011GL049971.

Smith, W. H. F., and P. Wessel (1990), Gridding with continuous curvature splines in tension, *Geophysics*, *55*, 293–305, doi:10.1190/1.1442837.

Tavakoli, F. (2007), Present-day deformation and kinematics of the active faults observed by GPS in the Zagros and east of Iran, PhD thesis, Univ. Joseph Fourier, Grenoble, France.

Tchalenko, J. S. (1975), Seismicity and structure of the Kopet Dagh (Iran, U.S.S.R.), *Philos. Trans. R. Soc. London Ser. A*, *278*, 1–28, doi:10.1098/rsta.1975.0019.

Trifonov, V. G. (1971), The pulse-like character of tectonic movements in regions of most recent mountain building (Kopet Dagh and Southeast Caucasus) [in Russian], *Geotectonics*, *4*, 234–235.

Trifonov, V. G. (1978), Late Quaternary tectonic movements of western and central Asia, *Geol. Soc. Am. Bull.*, *89*, 1059–1072.

Vernant, P., et al. (2004), Present-day crustal deformation and plate kinematics in the Middle East constrained by GPS measurements in Iran and northern Oman, *Geophys. J. Int.*, *157*, 381–398, doi:10.1111/j.1365-246X.2004.02222.x.

Wadge, G., et al. (2002), Atmospheric models, GPS and InSAR measurements of the tropospheric water vapour field over Mount Etna, *Geophys. Res. Lett.*, *29*(19), 1905, doi:10.1029/2002GL015159.

Walker, R. T., P. Gans, M. B. Allen, J. Jackson, M. Khatib, N. Marsh, and M. Zarrinkoub (2009), Late Cenozoic volcanism and rates of active faulting in eastern Iran, *Geophys. J. Int.*, *177*(2), 783–805, doi:10.1111/j.1365-246X.2008.04024.x.

Wang, H., T. J. Wright, and J. Biggs (2009), Interseismic slip rate of the northwestern Xianshuihe fault from InSAR data, *Geophys. Res. Lett.*, *36*, L03302, doi:10.1029/2008GL036560.

Wessel, P., and W. H. F. Smith (1998), New, improved version of generic mapping tools released, *Eos Trans. AGU*, *79*, 579–579, doi:10.1029/98EO00426.

Williams, S., Y. Bock, and P. Fang (1998), Integrated satellite interferometry: Tropospheric noise, GPS estimates and implications for interferometric synthetic aperture radar products, *J. Geophys. Res.*, *103*, 27,051–27,068, doi:10.1029/98JB02794.

Wright, T., B. Parsons, and E. Fielding (2001), Measurement of interseismic strain accumulation across the North Anatolian Fault by satellite radar interferometry, *Geophys. Res. Lett.*, *28*, 2117–2120, doi:10.1029/2000GL012850.

Xu, W. B., Z. W. Li, X. L. Ding, and J. J. Zhu (2011), Interpolating atmospheric water vapor delay by incorporating terrain elevation information, *J. Geod.*, *85*, 555–564, doi:10.1007/s00190-011-0456-0.

Zebker, H. A., P. A. Rosen, and S. Hensley (1997), Atmospheric effects in interferometric synthetic aperature radar surface deformation and topographic maps, *J. Geophys. Res.*, *102*, 7547–7564, doi:10.1029/96JB03804.

Zhu, M., G. Wadge, R. J. Holley, I. N. James, P. A. Clark, C. Wang, and M. J. Woodage (2007), High-resolution forecast models of water vapor over mountains: Comparison with MERIS and Meteosat data, *IEEE Geosci. Remote Sens. Lett.*, *4*, 401–405, doi:10.1109/LGRS.2007.895884.